Journal of Mathematical Modeling
Vol. -, No. -, 2026, pp. -. Research Article

JMM

Finite element modal analysis of two-dimensional heterogeneous elastic structures with variable material parameters

Hamzah Bakhti*, **Najat Magouh**

M2CS, STIS Research Center, ENSAM, Mohammed V University in Rabat, 10100, Rabat, Morocco

Email(s): h.bakhti@um5r.ac.ma, najat_magouh@um5.ac.ma

Abstract. The finite element method is used for the modal analysis of two-dimensional composite elastic structures with space-dependent material parameters. The scope is limited to two-dimensional, linear, isotropic, perfectly bonded composites under plane strain. The numerical examples represent multilayer and particle-reinforced composites with explicitly resolved particle regions, while the formulation also permits smoothly varying coefficients for functionally graded materials. The study combines variable-material modeling and finite element modal analysis within a unified framework. The elastodynamic problem is formulated in weak form, and the properties of the associated variable-coefficient elasticity operator are established under standard assumptions. The dynamic model is then approximated using finite elements to study the effects of geometric and material properties on the natural frequencies and mode shapes. A mesh-refinement study confirms convergence of the first six frequencies and stability of the associated mode shapes. A global bending-frequency consistency check is performed against the Euler–Bernoulli solution for a homogeneous clamped–clamped layer, while the heterogeneous cases are treated as parametric applications. For the prescribed multilayer configurations, the computed frequencies increase with the stiffness or thickness ratio and decrease with the density ratio. For the particle-reinforced composite, the two-dimensional particle area fraction produces a non-monotonic frequency response, which is interpreted qualitatively in terms of the stiffness–inertia balance. These findings demonstrate the ability of the proposed model to capture the main modal features of heterogeneous elastic structures.

Keywords: Finite element method, modal analysis, heterogeneous elastic structures, composite materials, natural frequencies and vibration modes.
AMS Subject Classification 2010: 35Q74, 65M60, 35J40, 74S05.

*Corresponding author
Received: 26 May 2026/ Revised: 07 September 2026/ Accepted: 08 September 2026
DOI: 10.22124/jmm.2026.33701.3096

 http://jmm.guilan.ac.ir

1 Introduction

Composite and multilayer elastic structures are widely used in modern engineering applications because they combine low weight with enhanced mechanical performance. In practical configurations such as layered panels [24], sandwich structures [9], coatings [15], and particle-reinforced components [37], the geometry and material properties affect the vibration response. Modal analysis therefore helps predict structural behaviour and supports the reliable design of heterogeneous elastic structures [10, 21]. Classical beam and plate theories, including Euler–Bernoulli beam theory [33], provide useful analytical insight for simple homogeneous configurations. The vibration modes and natural frequencies of more general systems, including multilayer structures and composites, are commonly approximated using finite element methods [24, 27, 35]; their modal characteristics may be significantly influenced by Young's modulus [21], density [4], and thickness [8].

The study of such models involves both theoretical and numerical considerations. Weak formulations, well-posedness results, and classical beam and plate theories provide the mathematical basis for describing elastic vibrations with variable material parameters [5, 6, 14, 30]. In previous related work, Magouh et al. [23] developed semi-analytical static and dynamic solutions for functionally graded electro-elastic multilayered plates. The present study continues the investigation of multilayer dynamics through a full two-dimensional finite element modal formulation for elastic structures with explicitly prescribed material regions. Natural frequencies and mode shapes are commonly approximated using finite element and related discretization techniques [18, 27, 34, 35]. Recent studies have addressed functionally graded hybrid shells and plates, porous graded solids, short-fiber composites, fiber–metal laminates, and stochastic free vibration of bidirectionally graded plates [11, 12, 16, 26, 28, 36].

Other computational developments include multiscale finite element methods, which incorporate fine material variations into coarse-scale basis functions [13]. Reduced-order models based on proper orthogonal decomposition reduce the computational dimension of structural dynamic systems [17]. Experimental modal testing has also been combined with numerical modelling to validate the natural frequencies of composite structures [31], while machine-learning methods have been proposed for the automatic identification of natural frequencies and mode shapes from measured structural responses [22, 25]. However, these approaches are generally specialized to particular structural theories, reinforcement architectures, computational objectives, or experimental and data-driven settings. Within this context, the present work combines established variable-material modeling, mathematical analysis, finite element error estimates, and comparative multilayer and particle-reinforced applications in a single framework with explicitly defined material regions. The multiscale, reduced-order, experimental, and data-driven approaches complement the present deterministic full-order formulation and represent relevant directions for future extension and validation.

Accordingly, this work applies the finite element method to the modal analysis of two-dimensional multilayer and composite elastic structures with spatially varying material parameters. The numerical examples use linear isotropic materials under plane strain and assume perfect bonding at internal interfaces. The elastodynamic problem is formulated in weak form, the properties of the associated elasticity operator are established, and the finite element approximation is derived. The influence of key physical parameters on the first natural frequencies and mode shapes is then investigated. A homogeneous clamped–clamped layer provides a consistency check, after which two-layer and particle-reinforced configurations are examined through parametric studies.

2 Mathematical formulation

2.1 Governing equations

An elastic body described in the Cartesian coordinate system (O,x,y) is considered. The spatial position is given by the vector $\mathbf{x} = (x,y)$, and the displacement from the reference configuration to the current deformed configuration in the domain $\Omega \subset \mathbb{R}^2$ is denoted by $\mathbf{u}(\mathbf{x},t) = (u_1,u_2)$. Here, time is represented by t. Small deformations are assumed, i.e. $\left|\dfrac{\partial u_i}{\partial x_j}\right| \ll 1$, so that the linear elasticity framework can be used [6, 14, 19]. This assumption is suitable for low-amplitude modal analysis about the undeformed equilibrium state.

Residual stresses and thermal effects are neglected in the present model. This provides a baseline model for initially stress-free components; prestressed, thermally loaded, or large-amplitude applications require an extended formulation.

For a heterogeneous composite material, spatial variations in the mechanical properties are represented by the density and Lamé parameters $\rho(x)$, $\lambda(x)$, and $\mu(x)$. These functions may be piecewise constant or smoothly varying according to the material microstructure [6, 30]. The density is assumed to satisfy $0 < \rho_{\min} \le \rho(x) \le \rho_{\max}$ almost everywhere in Ω.

In the reported numerical examples, these coefficients are piecewise constant over known layer, matrix, and particle subdomains. Smooth deterministic functions may instead be prescribed for a functionally graded material. More precisely, if $\Omega = \bigcup_{r=1}^{N_m} \overline{\Omega}_r$ is the partition into homogeneous material regions, the distribution used for each parameter $q \in \{\rho,\lambda,\mu\}$ is

$$q(x) = \sum_{r=1}^{N_m} q_r \chi_{\Omega_r}(x), \tag{1}$$

where χ_{Ω_r} equals one in Ω_r and zero elsewhere. This phase-indicator law represents the sharp interfaces of conventional laminates and particulate composites.

The linear elastodynamic equations are written as [6, 14, 19]:

$$\begin{aligned}
\rho(x)\ddot{u} - \nabla\cdot\sigma &= f, && \text{in } \Omega\times\mathscr{I}, && (2)\\
\sigma &= 2\mu(x)\varepsilon(u) + \lambda(x)(\nabla\cdot u)\mathbf{I}, && \text{in } \Omega\times\mathscr{I}, && (3)\\
u &= 0, && \text{on } \Gamma_D\times\mathscr{I}, && (4)\\
\sigma\cdot n &= g_N, && \text{on } \Gamma_N\times\mathscr{I}, && (5)\\
u &= u_0, && \text{in } \Omega,\ \text{for } t=0 && (6)\\
\dot{u} &= v_0, && \text{in } \Omega,\ \text{for } t=0 && (7)
\end{aligned}$$

Here, $\mathscr{I}$ is the time interval, $\mathbf{I}$ is the identity tensor, and the spatial dependence of the Lamé parameters λ and μ represents material heterogeneity. The Dirichlet and Neumann parts of the boundary are denoted by Γ_D and Γ_N, respectively.

The present constitutive law is linear and isotropic; anisotropy, including fiber-reinforced behaviour, can be introduced through $\sigma = \mathbb{C}(x) : \varepsilon(u)$, where $\mathbb{C}(x)$ is a spatially varying stiffness tensor. Nonlinear material behaviour would require tangent-stiffness linearization about an equilibrium configuration or a nonlinear modal-analysis formulation.

With small displacement gradients, the deformation is measured by the strain tensor, defined as [6,19]

$$\varepsilon = \frac{1}{2}\left(\nabla u + \nabla u^T\right) \tag{8}$$

or, in component form,

$$\varepsilon_{ij} = \frac{1}{2}\left(\frac{\partial u_i}{\partial x_j} + \frac{\partial u_j}{\partial x_i}\right). \tag{9}$$

2.2 Boundary conditions

For all numerical examples, the structure occupies a rectangular domain $\Omega = (0,L)\times(0,H)$, where H denotes the total thickness of the considered configuration. The vertical ends are clamped, while the upper and lower external surfaces are traction-free. Accordingly, the boundary decomposition is

$$\Gamma_D = \{(x,y) : x = 0 \text{ or } x = L,\ 0 \le y \le H\},$$

$$\Gamma_N = \{(x,y) : 0 < x < L,\ y = 0 \text{ or } y = H\}.$$

Both displacement components vanish on the clamped boundaries,

$$u_x = 0, \qquad u_y = 0 \qquad \text{on } \Gamma_D,$$

and the homogeneous Neumann condition is imposed on the remaining external boundary,

$$\sigma \cdot n = 0 \qquad \text{on } \Gamma_N.$$

For the multilayer and particle-reinforced configurations, the internal material interfaces are assumed to be perfectly bonded and are not included in Γ_N.

2.3 Weak formulation

For the weak formulation of (2)–(3), the Hilbert space is introduced as [3, 6, 19]

$$V = \left\{ v \in \left[H^1(\Omega)\right]^2 : v|_{\Gamma_D} = 0 \right\}. \tag{10}$$

The tensor contraction operator : is given by

$$A : B = \sum_{i,j=1}^{2} A_{ij} B_{ij} \tag{11}$$

for any two matrices A and B. The following relation is then obtained:

$$\sigma : \nabla v = \sigma : \varepsilon(v) \tag{12}$$

By applying the divergence theorem and Green's identity, together with the Neumann condition $\sigma \cdot n = g_N$ on Γ_N and the condition $v = 0$ on Γ_D, the following weak form is obtained: find $u : \mathscr{I} \to V$ such that

$$m(\ddot{u}, v) + a(u, v) = l(v) \quad \forall v \in V, \tag{13}$$

where the displacement $u = u(\mathbf{x},t)$ satisfies $u(\cdot,t) \in V$ for each $t \in \mathscr{I}$, and $\ddot{u}$ denotes the second time derivative of u. The stiffness and mass bilinear forms $a(\cdot,\cdot)$ and $m(\cdot,\cdot)$ and the linear functional $l(\cdot)$ are given by

$$\begin{aligned} a(u,v) &= 2(\mu(x)\varepsilon(u) : \varepsilon(v)) + (\lambda(x)\nabla\cdot u, \nabla\cdot v), \\ l(v) &= (f,v) + (g_N,v)_{\Gamma_N}, \\ m(w,v) &= \int_\Omega \rho(x) w\cdot v\, d\mathbf{x}. \end{aligned} \tag{14}$$

2.4 Existence and uniqueness

The continuity and coercivity of the spatial elasticity operator in (13) are established next. For each fixed load, the Lax–Milgram theorem applies once $a(\cdot,\cdot)$ is shown to be continuous and coercive on V and $l(\cdot)$ is shown to be continuous. The theorem below concerns the associated elliptic spatial problem, not the full dynamic initial-value problem.

Theorem 1. *Suppose that Γ_D has positive boundary measure and that $\mu,\lambda \in L^\infty(\Omega)$, with $\mu(x) \geq \mu_0 > 0$ and $\lambda(x) \geq 0$ almost everywhere in Ω. Let $f \in [L^2(\Omega)]^2$ and $g_N \in [L^2(\Gamma_N)]^2$. Then the associated elliptic variational problem has a unique solution $u \in V$ such that*

$$a(u,v) = l(v), \qquad \forall v \in V, \tag{15}$$

where

$$a(u,v) = 2(\mu(x)\varepsilon(u),\varepsilon(v)) + (\lambda(x)\nabla\cdot u, \nabla\cdot v), \qquad l(v) = (f,v) + (g_N,v)_{\Gamma_N}.$$

The following classical inequality is used to establish coercivity of the bilinear form [3, 6, 19].

Theorem 2 (Korn's inequality)**.** *There is a constant $C > 0$ such that, for each $v \in V$,*

$$\|\varepsilon(v)\|^2 \geq C\|v\|_V^2. \tag{16}$$

Proof of Theorem 1. Let $u,v \in V$. Since μ and λ are essentially bounded, the following estimate is obtained from the Cauchy–Schwarz inequality:

$$\begin{aligned} |a(u,v)| &\leq 2\|\mu\|_{L^\infty(\Omega)} \|\varepsilon(u)\|\,\|\varepsilon(v)\| + \|\lambda\|_{L^\infty(\Omega)} \|\nabla\cdot u\|\,\|\nabla\cdot v\| \\ &\leq C\|u\|_V\|v\|_V, \end{aligned} \tag{17}$$

so $a(\cdot,\cdot)$ is continuous on $V \times V$.

For the linear functional, the following estimate is obtained by combining the trace theorem with the Cauchy–Schwarz inequality:

$$\begin{aligned} |l(v)| &\leq \|f\|_{[L^2(\Omega)]^2}\|v\|_{[L^2(\Omega)]^2} + \|g_N\|_{[L^2(\Gamma_N)]^2}\|v\|_{[L^2(\Gamma_N)]^2} \\ &\leq C\left(\|f\|_{[L^2(\Omega)]^2} + \|g_N\|_{[L^2(\Gamma_N)]^2}\right)\|v\|_V, \end{aligned} \tag{18}$$

hence l is continuous on V.

It remains to establish coercivity. Using $\mu(x) \geq \mu_0 > 0$ and $\lambda(x) \geq 0$, the following inequality is obtained:

$$a(v,v) = 2(\mu\varepsilon(v),\varepsilon(v)) + (\lambda\nabla\cdot v, \nabla\cdot v) \geq 2\mu_0\|\varepsilon(v)\|^2. \tag{19}$$

By Korn's inequality, there exists a constant $C > 0$ such that

$$\|\varepsilon(v)\|^2 \geq C\|v\|_V^2, \qquad \forall v \in V. \tag{20}$$

Therefore,

$$a(v,v) \geq 2\mu_0 C\|v\|_V^2, \qquad \forall v \in V, \tag{21}$$

which proves the coercivity of $a(\cdot,\cdot)$ on V.

Since $a(\cdot,\cdot)$ is continuous and coercive on V, while $l(\cdot)$ is continuous on V, the Lax–Milgram theorem ensures the existence of a unique element $u \in V$ satisfying

$$a(u,v) = l(v), \qquad \forall v \in V.$$

This establishes the unique solution of the associated elliptic variational problem. For the dynamic problem, if $0 < \rho_{\min} \leq \rho(x) \leq \rho_{\max}$ almost everywhere, $u_0 \in V$, $v_0 \in [L^2(\Omega)]^2$, and the time-dependent load belongs to $L^2(\mathscr{I};V')$, standard second-order evolution theory gives a unique weak solution. $\square$

The continuity and coercivity of $a(\cdot,\cdot)$ and the positivity of $m(\cdot,\cdot)$ provide the analytical basis for the continuous and discrete eigenvalue problems. The conditional approximation estimates are then assessed numerically through the mesh-refinement study.

3 Finite element discretization

3.1 Spatial discretization

The weak problem (13) is approximated using finite elements [1, 14, 19, 38]. Let $\mathscr{K} = \{K\}$ be a shape-regular triangular mesh on Ω, and let V_h be the polynomial space

$$V_h = \left\{ v \in V : v|_K \in [P_1(K)]^2, \forall K \in \mathscr{K} \right\}. \tag{22}$$

This space consists of displacement vectors whose components are continuous, piecewise linear, and zero on Γ_D. The discrete finite element problem is stated as follows: find $u_h \in V_h$ such that

$$m(\ddot{u}_h, v_h) + a(u_h, v_h) = l(v_h), \quad \forall v_h \in V_h. \tag{23}$$

The three independent components of the stress tensor σ and strain tensor ε are represented by

$$\sigma = [\sigma_{11} \;\; \sigma_{22} \;\; \sigma_{12}]^T \tag{24}$$

and

$$\varepsilon = [\varepsilon_{11} \;\; \varepsilon_{22} \;\; 2\varepsilon_{12}]^T. \tag{25}$$

Thus, Hooke's law is expressed in matrix form as

$$\sigma = C(x)\varepsilon \tag{26}$$

with the matrix $C(x)$ defined as

$$C(x) = \begin{bmatrix} \lambda(x)+2\mu(x) & \lambda(x) & 0 \\ \lambda(x) & \lambda(x)+2\mu(x) & 0 \\ 0 & 0 & \mu(x) \end{bmatrix}. \tag{27}$$

The reported two-dimensional computations use the plane-strain assumption. In each material region, Young's modulus E and Poisson's ratio ν are converted to the Lamé parameters through

$$\lambda = \frac{E\nu}{(1+\nu)(1-2\nu)}, \qquad \mu = \frac{E}{2(1+\nu)}.$$

Thus, the matrix in (27) is the plane-strain constitutive matrix; plane stress would require a different constitutive matrix and is not considered here.

Because the stress and strain tensors considered here are symmetric, the following expression is obtained:

$$a(u_h, v) = \int_\Omega \varepsilon^T(v) C(x) \varepsilon(u_h)\, d\mathbf{x}. \tag{28}$$

The finite element approximation $u_h \in V_h$ is written in matrix form as

$$u_h = \begin{bmatrix} u_1 \\ u_2 \end{bmatrix}_h = \begin{bmatrix} \varphi_1 & 0 & \varphi_2 & 0 & \dots & \varphi_{n_i} & 0 \\ 0 & \varphi_1 & 0 & \varphi_2 & \dots & 0 & \varphi_{n_i} \end{bmatrix} \begin{bmatrix} d_{11} \\ d_{12} \\ d_{21} \\ d_{22} \\ \vdots \\ d_{n_i 1} \\ d_{n_i 2} \end{bmatrix} = \varphi d(t), \tag{29}$$

where φ_i, $i = 1, 2, \dots, n_i$, are the hat basis functions, $d(t)$ is the time-dependent vector of nodal displacements, and n_i is the number of unconstrained nodes.

The strain field is related to the displacement field through

$$\begin{bmatrix} \varepsilon_{11} \\ \varepsilon_{22} \\ 2\varepsilon_{12} \end{bmatrix} = \begin{bmatrix} \partial/\partial x_1 & 0 \\ 0 & \partial/\partial x_2 \\ \partial/\partial x_2 & \partial/\partial x_1 \end{bmatrix} \begin{bmatrix} u_1 \\ u_2 \end{bmatrix}. \tag{30}$$

Introducing the corresponding strain matrix gives

$$B = \begin{bmatrix} \partial/\partial x_1 & 0 \\ 0 & \partial/\partial x_2 \\ \partial/\partial x_2 & \partial/\partial x_1 \end{bmatrix} \begin{bmatrix} \varphi_1 & 0 & \varphi_2 & 0 & \dots & \varphi_{n_i} & 0 \\ 0 & \varphi_1 & 0 & \varphi_2 & \dots & 0 & \varphi_{n_i} \end{bmatrix}. \tag{31}$$

The discrete strain and stress fields are then obtained as

$$\begin{aligned} \varepsilon &= Bd(t), \\ \sigma &= C(x)Bd(t). \end{aligned} \tag{32}$$

The following matrix system is obtained from the finite element discretization:

$$M\ddot{d} + Kd = F(t), \tag{33}$$

where the $2n_i \times 2n_i$ mass and stiffness matrices are denoted by M and K, respectively:

$$M = \int_\Omega \rho(x)\varphi^T \varphi\, d\mathbf{x}, \tag{34}$$

$$K = \int_\Omega B^T C(x) B\, d\mathbf{x}. \tag{35}$$

The $2n_i \times 1$ load vector is

$$F = \int_\Omega \varphi^T f\, d\mathbf{x} + \int_{\Gamma_N} \varphi^T g_N\, ds. \tag{36}$$

The integrals that define the mass matrix, stiffness matrix, and load vector are evaluated using higher-order Gauss quadrature over triangular elements [7].

3.2 Modal analysis

At the continuous level, the free-vibration eigenproblem is to find an eigenpair (ω_j, ϕ_j), with $\phi_j \in V \setminus \{0\}$, such that

$$a(\phi_j, v) = \omega_j^2 m(\phi_j, v), \qquad \forall v \in V. \tag{37}$$

The corresponding finite element eigenpair is denoted by $(\omega_{j,h}, \phi_{j,h})$.

For free vibration, $F(t) = 0$, and a harmonic solution of (33) is sought in the form

$$d(t) = q_j \sin(\omega_{j,h} t),$$

where q_j is the nodal vector associated with $\phi_{j,h}$ and $\omega_{j,h}$ is the discrete natural frequency. Substitution into (33) gives the generalized algebraic eigenvalue problem

$$Kq_j = \omega_{j,h}^2 M q_j.$$

Thus, $\omega_{j,h}^2$ is the discrete eigenvalue.

For any nonzero modal vector q, the Rayleigh quotient is defined by

$$\mathscr{R}(q) = \frac{q^T K q}{q^T M q}. \tag{38}$$

For a discrete eigenmode q_j, $\mathscr{R}(q_j) = \omega_{j,h}^2$, showing that each natural frequency is governed by the balance between modal stiffness and modal mass.

3.3 Numerical implementation

The finite element assembly, generalized eigenvalue solution, and post-processing were implemented in MATLAB. After application of the Dirichlet boundary conditions, the stiffness and mass matrices are real, sparse, and symmetric, and the mass matrix is positive definite. The first ten eigenpairs were computed using a restarted Lanczos-type Krylov subspace method [20, 32], and the first six eigenpairs were retained for the reported results. The smallest-magnitude option corresponds to a shift-and-invert spectral transformation with zero shift. This transformation targets the eigenvalues nearest zero and therefore the lowest natural frequencies. Since only the lowest modes were required, no nonzero shift was used to target interior or higher eigenvalues.

The eigensolver iteration was accepted when its residual convergence criterion was satisfied for all requested eigenpairs; convergence with respect to spatial discretization is examined separately in Section 4.1. The consistent mass matrix defined by the finite element integral above was used without mass lumping. The eigenvectors were mass-normalized so that $q_i^T M q_j = \delta_{ij}$.

The specified geometries were discretized using shape-regular conforming triangular meshes with continuous piecewise-linear displacement functions. The maximum element sizes used in the numerical cases are stated with the corresponding results. Material coefficients were assigned according to the prescribed material subdomains. A triangular Gaussian quadrature rule exact for at least quadratic polynomial integrands was used; it therefore integrates the consistent mass and stiffness contributions of the piecewise-linear elements with piecewise-constant material coefficients.

For a mesh with n_i unconstrained nodes, the algebraic system contains $2n_i$ active displacement degrees of freedom. Complete per-mesh timing and hardware records were not retained, so no estimated computational-cost values are reported.

3.4 Error estimates

Assume that the element integrals defining the stiffness form are evaluated with a quadrature rule accurate enough to preserve Galerkin orthogonality. The accuracy of the finite element solution u_h is assessed through the error $e = u - u_h$, leading to the following conditional a priori estimate.

Theorem 3 (Conditional a priori estimate [19])**.** *Assume that the mesh resolves the material interfaces and that $u|_{\Omega_r} \in [H^2(\Omega_r)]^2$ for every material subdomain Ω_r. Then the finite element solution u_h satisfies*

$$\|\nabla e\| \leq Ch \left(\sum_{r=1}^{N_m} |u|^2_{H^2(\Omega_r)} \right)^{1/2} \tag{39}$$

where C is independent of u, u_h, and the mesh size h.

For an interface-fitted mesh, a residual indicator can be defined element-wise by

$$\eta_K^2 = h_K^2 \|f + \nabla \cdot \sigma_h\|^2_{0,K} + \frac{h_K}{2} \|[\![\sigma_h \cdot n]\!]\|^2_{0,\partial K \setminus \partial\Omega} + h_K \|g_N - \sigma_h \cdot n\|^2_{0,\partial K \cap \Gamma_N}.$$

Here, $[\![\sigma_h \cdot n]\!]$ denotes the traction jump across an interior element edge. This expression is used only as a residual indicator; no reliability or efficiency bound is claimed for discontinuous coefficients and material interfaces.

For an isolated eigenmode satisfying the stated piecewise H^2 regularity, classical conforming finite element eigenvalue theory gives a first-order eigenfunction error in the energy norm for the piecewise-linear space V_h and a second-order eigenvalue error [2]:

$$\|\phi_j - \phi_{j,h}\|_a = O(h), \qquad |\omega_j^2 - \omega_{j,h}^2| = O(h^2).$$

Table 1: Mesh-convergence study for the first six natural frequencies and their observed convergence rates

$h_{\max}$	Mode 1		Mode 2		Mode 3		Mode 4		Mode 5		Mode 6	
	Frequency	Rate	Frequency	Rate	Frequency	Rate	Frequency	Rate	Frequency	Rate	Frequency	Rate
$L/2^5$	0.020353	–	0.058991	–	0.11897	–	0.1995	–	0.29934	–	0.33009	–
$L/2^6$	0.016273	−0.95	0.044822	−0.62	0.087692	−0.45	0.14449	−0.35	0.2149	−0.30	0.29846	−2.18
$L/2^7$	0.0083694	2.86	0.023048	2.86	0.045124	2.86	0.07447	2.86	0.11103	2.85	0.15471	2.84
$L/2^8$	0.0072828	1.53	0.020056	1.54	0.03927	1.53	0.064812	1.53	0.096631	1.53	0.13467	1.53
$L/2^9$	0.0069068	1.87	0.019026	1.83	0.037246	1.85	0.061473	1.84	0.091642	1.85	0.12771	1.85
$L/2^{10}$	0.0068037	–	0.018736	–	0.036683	–	0.06054	–	0.09026	–	0.12578	–

Since $\omega_j > 0$,

$$|\omega_j - \omega_{j,h}| = \frac{|\omega_j^2 - \omega_{j,h}^2|}{\omega_j + \omega_{j,h}} = O(h^2).$$

Thus, the first-order estimate concerns the eigenfunction in the energy norm, whereas the corresponding eigenvalue and frequency estimates are second order. The self-convergence rates in Section 4.1 are observed numerical rates and provide supporting evidence rather than a proof of these estimates.

4 Numerical results

This section presents numerical experiments that assess the finite element model and illustrate the influence of material and geometric parameters on the dynamic response of composite elastic structures. Figure 1 shows the three configurations considered: a single homogeneous layer, a two-layer structure, and a composite matrix with embedded particles. First, the FE approximation is compared with Euler–Bernoulli beam values for a homogeneous clamped–clamped layer [29, 33]. The effects of the stiffness ratio E_2/E_1, thickness ratio H_2/H_1, and density ratio ρ_2/ρ_1 on the first six natural frequencies and associated mode shapes are then examined for a two-layer clamped–clamped structure. Finally, the effect of particle content is studied for a composite elastic layer containing particles with different material properties. The homogeneous comparison provides a consistency check, whereas the two-layer and particle-reinforced cases are parametric studies without independent benchmarks. Both heterogeneous configurations are deterministic and explicitly prescribed; no stochastic sampling or micromechanical homogenization is used. Accordingly, the trends reported below are observations for the prescribed configurations rather than general theoretical conclusions. In the particle study, v_f denotes the two-dimensional particle area fraction; the particle regions are resolved explicitly rather than replaced by homogenized material properties.

No analytical or published two-layer benchmark matching the present geometry, boundary conditions, plane-strain assumption, and material parameters is used; consequently, the two-layer study is presented as a parametric application rather than an independently validated case.

4.1 Mesh convergence

A mesh-refinement study was performed by decreasing the maximum element size from $L/2^5$ to $L/2^{10}$. The first six frequencies progressively stabilize under refinement, as shown in Table 1, confirming numerical convergence. The associated mode shapes retain the same spatial patterns over the refined meshes, indicating modal stability.

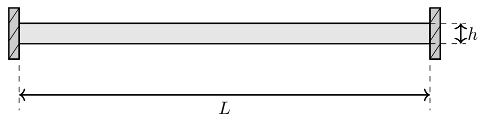

(a) Single homogeneous layer

(b) Two-layer structure

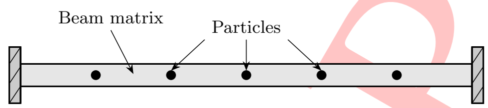

(c) Composite structure

Figure 1: Sketches of the three configurations studied in the numerical experiments.

The self-convergence rate uses frequency differences from three consecutive meshes. For mode j and mesh level k,

$$p_{j,k} = \frac{\log\left(\dfrac{|\omega_{j,k-1} - \omega_{j,k}|}{|\omega_{j,k} - \omega_{j,k+1}|}\right)}{\log 2}.$$

Here, $\omega_{j,k}$ is the frequency obtained with $h_{\max} = L/2^k$. The negative rates for the coarsest mesh triplet result from the increase in the consecutive frequency differences and indicate that these coarse meshes are outside the asymptotic range. The rates then become positive as the mesh is refined and range from 1.83 to 1.87 for the finest available mesh triplet. These values are close to the second-order frequency rate associated with the piecewise-linear eigenvalue approximation and are therefore consistent with the eigenproblem error estimates stated above.

4.2 Homogeneous consistency check

To check the finite element approximation, the first six natural frequencies of a homogeneous two-dimensional thin elastic layer with clamped–clamped boundary conditions are compared with Euler–Bernoulli beam-theory values. The layer has length $L = 10$ and thickness $H = 0.1$, and the finite element mesh has a maximum element size of $h_{\max} = 0.01$. The material is homogeneous and isotropic, with Young's modulus $E = 1$, Poisson's ratio $\nu = 0.3$, and density $\rho = 1$. As shown in Table 2, the FE frequencies agree closely with the analytical reference values for all six modes. The relative error is nearly uniform and decreases from approximately 5.34% for the first mode to 4.49% for the sixth mode. This difference should not be interpreted as discretization error alone: the plane-strain continuum includes transverse constraint and shear effects absent from classical Euler–Bernoulli theory. Mesh refinement reduces discretization error but does not eliminate these modeling differences; their individual contributions have not been quantified here. This agreement shows that the FE model captures the global dynamic behaviour and reproduces the expected frequency trend. Figures 2–3 show the first six mode shapes, whose deformation patterns are consistent with beam theory and exhibit an increasing number of

Table 2: First six natural frequencies of a homogeneous single layer with clamped–clamped boundary conditions

Mode	Beam Theory	FEM	Relative error
1	0.00646	0.00680	+5.34%
2	0.01780	0.01874	+5.24%
3	0.03490	0.03668	+5.10%
4	0.05769	0.06054	+4.94%
5	0.08619	0.09026	+4.73%
6	0.12037	0.12578	+4.49%

Table 3: Variation of the first six natural frequencies with the stiffness ratio E_2/E_1 for a two-layer clamped–clamped structure

E_2/E_1	Mode 1	Mode 2	Mode 3	Mode 4	Mode 5	Mode 6
0.5	0.00916	0.02516	0.04908	0.08061	0.11951	0.16547
1	0.01105	0.03034	0.05918	0.09721	0.14412	0.19957
2	0.01296	0.03559	0.06942	0.11406	0.16913	0.23425
5	0.01564	0.04295	0.08382	0.13778	0.20443	0.28332
10	0.01830	0.05028	0.09819	0.16149	0.23980	0.33261
20	0.02226	0.06118	0.11955	0.19676	0.29247	0.40606
50	0.03094	0.08509	0.16641	0.27412	0.40791	0.56696
100	0.04148	0.11408	0.22321	0.36782	0.54763	0.76156

nodal regions as the mode number increases.

4.3 Parametric studies

4.3.1 Effect of stiffness ratio

In the second case, a two-layer clamped–clamped elastic structure is considered, with material properties that are constant within each layer. Accordingly, $q(x) = q_1\chi_{\Omega_1}(x) + q_2\chi_{\Omega_2}(x)$, and the coefficients are discontinuous only across the bonded interface. The structure has length $L = 10$, equal layer thicknesses $H_1 = H_2 = 0.1$, and a maximum element size of $h_{\max} = 0.01$. The densities are $\rho_1 = 1$ and $\rho_2 = 2$, and Poisson's ratio is $\nu = 0.3$ in both layers. The first-layer Young's modulus is fixed at $E_1 = 1$, while E_2/E_1 is varied to examine the influence of stiffness contrast. As shown in Table 3, all six frequencies increase with E_2/E_1 in the reported cases, consistent with the greater stiffness produced by increasing the Young's modulus of the second layer. Figures 4 and 5 show that the overall first-mode pattern remains essentially unchanged across the investigated stiffness ratios.

4.3.2 Effect of thickness ratio

In the third case, the same two-layer clamped–clamped elastic structure is considered with $H_1 = 0.1$, while the thickness ratio H_2/H_1 is varied by changing the second-layer thickness H_2. The same mesh settings are used, and the material parameters remain fixed at $E_1 = 1$ and $E_2 = 2$. As shown in Table 4, all six natural frequencies increase with H_2/H_1 in the reported cases. Because H_2 is changed while H_1 is fixed, the total thickness, geometry, mass, and stiffness vary simultaneously; the observed trend therefore cannot be attributed to a single isolated effect. Figures 6 and 7 show that the overall first-mode pattern is

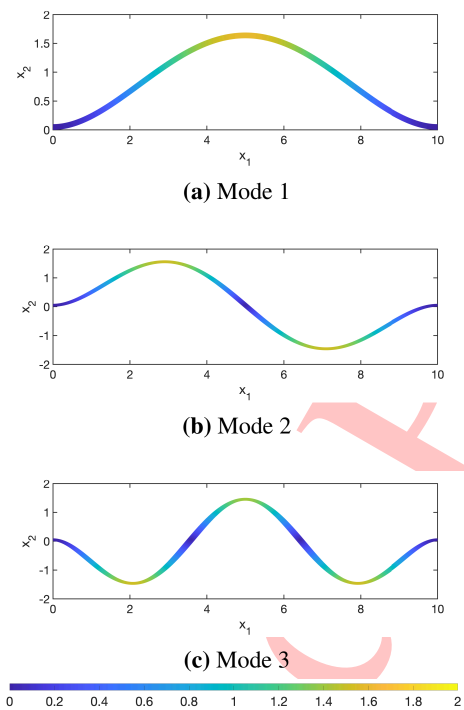

(a) Mode 1

(b) Mode 2

(c) Mode 3

Figure 2: Mode shapes 1–3 of the homogeneous single layer with clamped–clamped boundary conditions.

Table 4: Variation of the first six natural frequencies with the thickness ratio H_2/H_1 for a two-layer clamped–clamped structure.

H_2/H_1	Mode 1	Mode 2	Mode 3	Mode 4	Mode 5	Mode 6
0.1	0.00785	0.02162	0.04231	0.06978	0.10397	0.14476
0.25	0.00892	0.02455	0.04801	0.07912	0.11776	0.16377
0.5	0.01031	0.02834	0.05538	0.09117	0.13550	0.18816
1	0.01296	0.03559	0.06942	0.11406	0.16913	0.23425
2	0.01874	0.05130	0.09963	0.16280	0.23990	0.32965
3	0.024902	0.067804	0.13082	0.21208	0.30980	0.32990

preserved. Differences in the plotted magnitudes reflect the adopted mass normalization and should not be interpreted as physical vibration amplitudes.

4.3.3 Effect of density ratio

The effect of density contrast is examined using the same two-layer clamped–clamped structure, mesh, and remaining material and geometric parameters. As shown in Table 5, all six natural frequencies decrease as ρ_2/ρ_1 increases in the reported cases, a trend consistent with the greater modal inertia produced by increasing the density of the second layer. Figures 8 and 9 show that the overall first-mode pattern is preserved. Differences in the plotted magnitudes reflect the adopted mass normalization rather than physical vibration amplitudes.

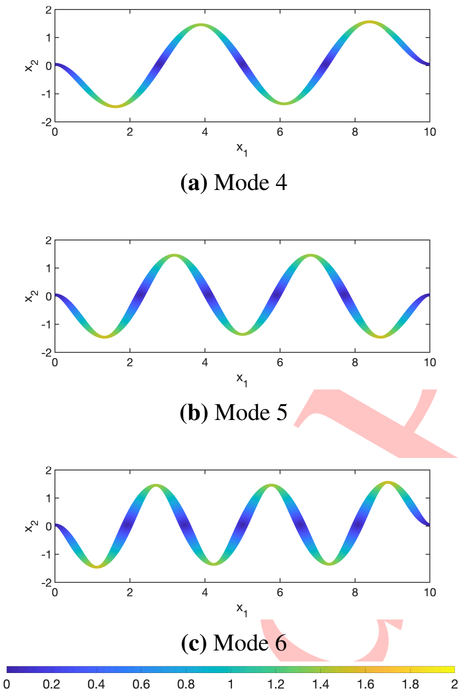

(a) Mode 4

(b) Mode 5

(c) Mode 6

Figure 3: Mode shapes 4–6 of the homogeneous single layer with clamped–clamped boundary conditions

Table 5: Variation of the first six natural frequencies with the density ratio ρ_2/ρ_1 for a two-layer clamped–clamped structure.

ρ_2/ρ_1	Mode 1	Mode 2	Mode 3	Mode 4	Mode 5	Mode 6
0.2	0.02048	0.05624	0.10970	0.18015	0.26708	0.36967
0.5	0.01832	0.05031	0.09814	0.16119	0.23898	0.33086
1	0.01587	0.04358	0.08501	0.13964	0.20705	0.28671
2	0.01296	0.03559	0.06942	0.11406	0.16913	0.23425
5	0.00916	0.02517	0.04910	0.08068	0.11964	0.16573
10	0.00677	0.01859	0.03627	0.05959	0.08838	0.12244

4.3.4 Particle-reinforced structure

In the final case, an elastic layer containing particles with different material properties is considered. The structure has length $L = 10$ and thickness $H = 0.2$. For nonzero particle area fractions, the structure contains 20 equally spaced particles. If Ω_m and Ω_p denote the matrix and particle regions, respectively, the implemented law is $q(x) = q_m\chi_{\Omega_m}(x) + q_p\chi_{\Omega_p}(x)$. The matrix has $E_1 = 1$ and $\rho_1 = 1$, while the particles have $E_2 = 10$ and $\rho_2 = 2$; Poisson's ratio is fixed at $\nu = 0.3$ for both materials. Here, the quantity denoted by v_f is the particle area fraction in the two-dimensional domain, and each particle region is represented explicitly by piecewise-constant coefficients. Table 6 reports the first six natural frequencies as functions of this fraction. For the prescribed configurations, the frequencies initially decrease and then increase, with only small variations; the stiffness–inertia explanation discussed below is qualitative and has not been demonstrated by a separate modal-energy decomposition. Figures 10

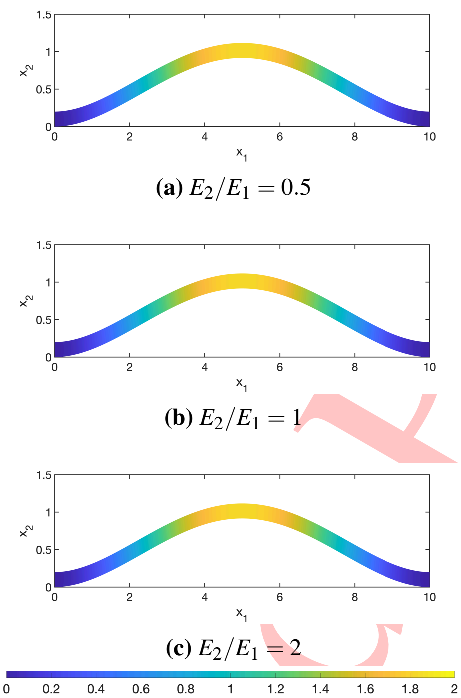

(a) $E_2/E_1 = 0.5$

(b) $E_2/E_1 = 1$

(c) $E_2/E_1 = 2$

Figure 4: First mode shapes obtained for different values of the stiffness ratio E_2/E_1 in the two-layer clamped–clamped structure: (a) $E_2/E_1 = 0.5$, (b) $E_2/E_1 = 1$, and (c) $E_2/E_1 = 2$, together with the corresponding color bar

Table 6: Variation of the first six natural frequencies with respect to the particle area fraction for the composite clamped–clamped structure.

v_f	Mode 1	Mode 2	Mode 3	Mode 4	Mode 5	Mode 6
0	0.01353	0.03716	0.07248	0.11905	0.17650	0.24439
0.05	0.01328	0.03649	0.07119	0.11700	0.17356	0.24046
0.1	0.01318	0.03621	0.07066	0.11615	0.17234	0.23884
0.15	0.01320	0.03625	0.07074	0.11628	0.17254	0.23915
0.2	0.01328	0.03649	0.0712	0.11703	0.17366	0.24070

and 11 show the same non-monotonic trend.

Because these particle-reinforced calculations have not been independently reproduced or benchmarked, the reported values are retained only as preliminary results for the prescribed discretized geometries and are not used to establish a general design rule.

5 Discussion

5.1 Physical interpretation

For the computed multilayer configurations, the frequency trends can be interpreted through the stiffness and mass terms in the Rayleigh quotient. Increasing E_2/E_1 is consistent with greater modal stiffness, while increasing ρ_2/ρ_1 is consistent with greater modal mass. In the thickness-ratio study, however,

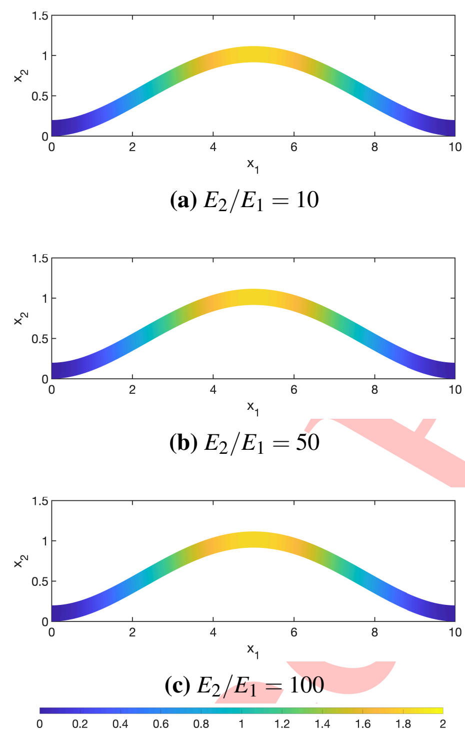

Figure 5: First mode shapes obtained for different values of the stiffness ratio E_2/E_1 in the two-layer clamped–clamped structure: (a) $E_2/E_1 = 10$, (b) $E_2/E_1 = 50$, and (c) $E_2/E_1 = 100$, together with the corresponding color bar

changing H_2 alters the total thickness, geometry, mass, and stiffness simultaneously. For the particle-reinforced configurations, the Rayleigh quotient provides a plausible qualitative stiffness–inertia interpretation of the non-monotonic response, but the proposed stiffness–inertia explanation has not been demonstrated quantitatively and should not be regarded as a general conclusion.

The particle-reinforced results should therefore be regarded as preliminary observations for the prescribed configurations and require independent numerical or experimental verification.

5.2 Design implications

Within the investigated configurations, the computed trends suggest that the modal response can be adjusted through the stiffness, thickness, and density parameters. These observations are configuration-specific: the thickness-ratio study combines several geometric and mechanical changes, and the particle-reinforced results require independent verification before they are used for design or optimization. The results are most directly relevant to layered panels and particle-reinforced components, while sandwich structures and functionally graded materials remain possible extensions that were not explicitly demonstrated.

For real composite structures, the model is most applicable as a first approximation when the response is dominated by small in-plane vibrations and the constituents may reasonably be treated as linear, isotropic, and perfectly bonded. Quantitative prediction of many engineering components would

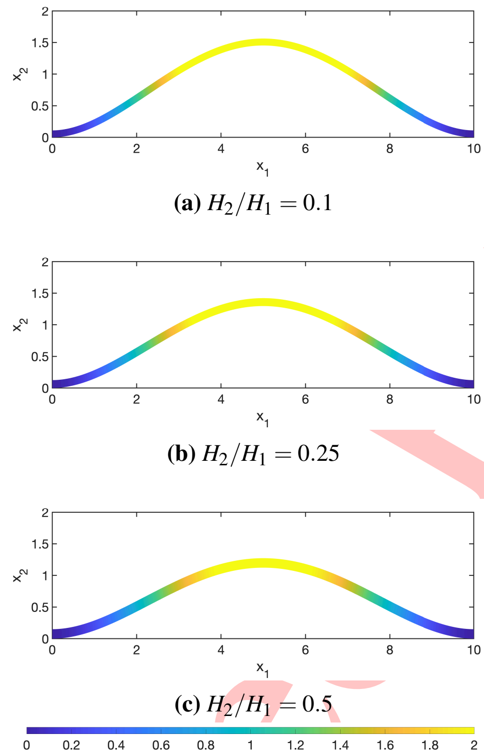

(a) $H_2/H_1 = 0.1$

(b) $H_2/H_1 = 0.25$

(c) $H_2/H_1 = 0.5$

Figure 6: First mode shapes obtained for different values of the thickness ratio H_2/H_1 in the two-layer clamped–clamped structure: (a) $H_2/H_1 = 0.1$, (b) $H_2/H_1 = 0.25$, and (c) $H_2/H_1 = 0.5$.

additionally require anisotropy, damping, imperfect interfaces, manufacturing variability, and three-dimensional effects.

5.3 Limitations

The model assumes linear isotropic elasticity, perfect bonding, and no damping, residual stress, or thermal loading. The plane-strain formulation excludes out-of-plane deformation and three-dimensional edge effects. Thin structures governed by plane stress require a different constitutive matrix, and general three-dimensional composite components are outside the scope of the model. The homogeneous case provides a global consistency check. The multilayer and particle-reinforced cases do not have independent benchmarks. A quantitative comparison with a homogenized model was not performed because no equivalent representative volume element or effective material law was defined for the particle geometries. The conclusions therefore apply to the prescribed two-dimensional geometries and material data.

6 Conclusion

This work presents a finite element model for the modal analysis of two-dimensional composite elastic structures with different material properties. The formulation is derived from the weak form of the elas-

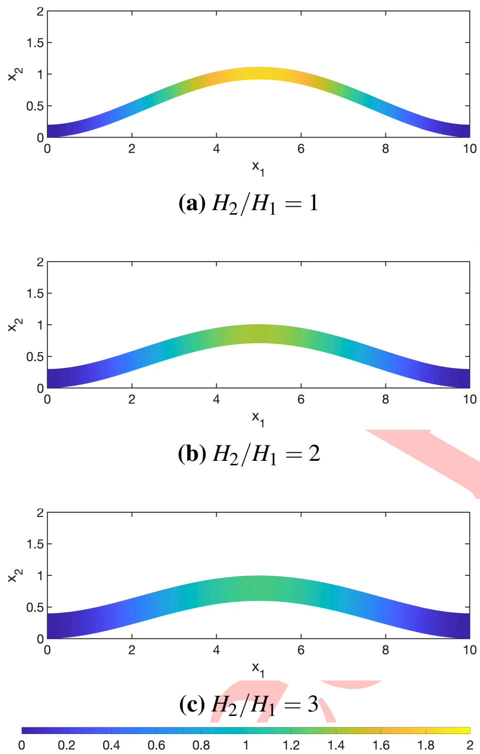

Figure 7: First mode shapes obtained for different values of the thickness ratio H_2/H_1 in the two-layer clamped–clamped structure: (a) $H_2/H_1 = 1$, (b) $H_2/H_1 = 2$, and (c) $H_2/H_1 = 3$.

todynamic problem and is used to compute the first natural frequencies and associated vibration modes for several material and geometric configurations. More specifically, the study formulates the variable-coefficient plane-strain eigenproblem, establishes the properties of its spatial operator, and derives a conforming finite element approximation with a consistent mass matrix.

The study combines established variable-material modeling, mathematical analysis, finite element error estimates, and comparative multilayer and particle-reinforced applications within the same modal framework. The non-monotonic particle response is treated as a preliminary observation for the prescribed configuration rather than as a general result. The reported applications concern deterministic multilayer and particle-reinforced composites. The particle regions are explicitly resolved in two dimensions and are not represented by a homogenized material law. Although the formulation can accommodate prescribed smooth gradation, stochastic microstructures require a separate probabilistic extension.

The verified evidence consists of the mesh-refinement behavior and the homogeneous Euler–Bernoulli consistency check. The two-layer trends are configuration-specific parametric observations, while the particle-reinforced results remain preliminary because neither heterogeneous case has an independent benchmark. For the prescribed two-layer configurations, the computed frequencies increase with the stiffness and thickness ratios and decrease with the density ratio. For the particle-reinforced layer, the frequencies vary non-monotonically with the two-dimensional particle area fraction; this preliminary trend and its qualitative stiffness–inertia interpretation require independent verification.

These findings show that the model captures the main dynamic features of multilayer and com-

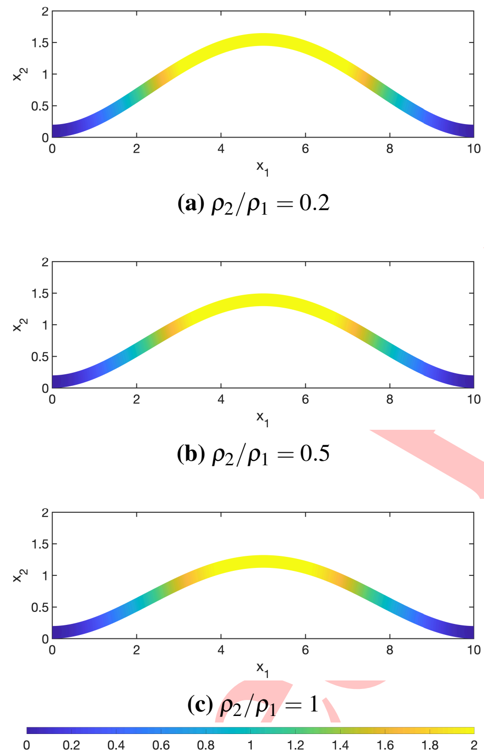

(a) $\rho_2/\rho_1 = 0.2$

(b) $\rho_2/\rho_1 = 0.5$

(c) $\rho_2/\rho_1 = 1$

Figure 8: First mode shapes obtained for different values of the density ratio ρ_2/ρ_1 in the two-layer clamped–clamped structure: (a) $\rho_2/\rho_1 = 0.2$, (b) $\rho_2/\rho_1 = 0.5$, and (c) $\rho_2/\rho_1 = 1$.

posite elastic structures and provides a computational tool for understanding how material distribution affects vibration behaviour. The model is relevant to the design and optimization of layered and particle-reinforced structures for which accurate prediction of modal characteristics is essential.

Future work may consider more general boundary conditions and more complex multilayer geometries, as well as damping, anisotropic or viscoelastic materials, and fully heterogeneous spatial distributions of the elastic coefficients. Residual stresses, thermal strains, and temperature-dependent material properties could also be incorporated to study modal behaviour under variable-temperature conditions. Further developments may include a quantitative comparison with a homogenized model based on an equivalent representative volume element, transient dynamic simulations, experimental validation, and optimization of multilayer or composite configurations for targeted vibrational properties.

Conflict of interest

The authors declare that they have no conflicts of interest related to this work.

Funding

This research received no external funding.

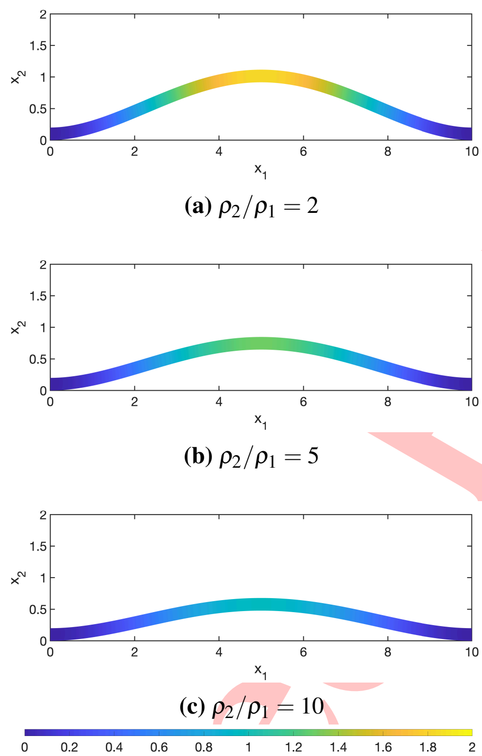

(a) $\rho_2/\rho_1 = 2$

(b) $\rho_2/\rho_1 = 5$

(c) $\rho_2/\rho_1 = 10$

Figure 9: First mode shapes obtained for different values of the density ratio ρ_2/ρ_1 in the two-layer clamped–clamped structure: (a) $\rho_2/\rho_1 = 2$, (b) $\rho_2/\rho_1 = 5$, and (c) $\rho_2/\rho_1 = 10$.

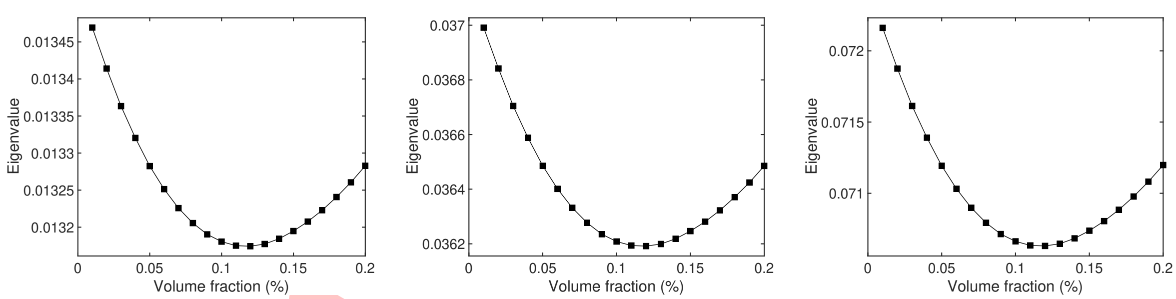

(a) Mode 1

(b) Mode 2

(c) Mode 3

Figure 10: Variation of the first six natural frequencies with respect to the particle area fraction in the composite clamped–clamped structure: (a) Mode 1, (b) Mode 2, and (c) Mode 3.

Acknowledgments

The authors thank the editor and reviewers for their constructive comments and suggestions, which helped improve the manuscript.

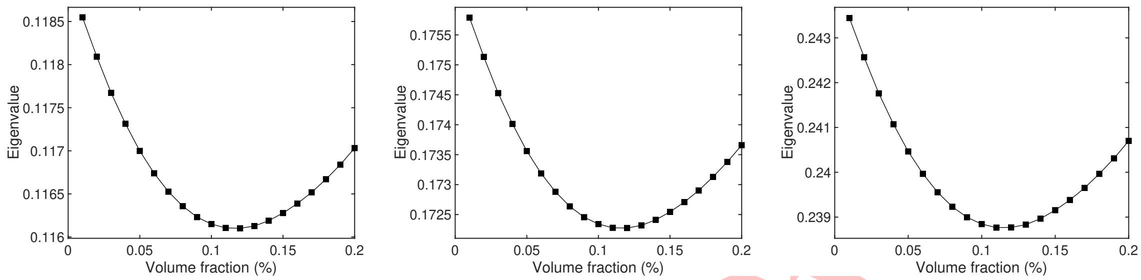

(a) Mode 4 **(b)** Mode 5 **(c)** Mode 6

Figure 11: Variation of the first six natural frequencies with respect to the particle area fraction in the composite clamped–clamped structure: (a) Mode 4, (b) Mode 5, and (c) Mode 6.

References

[1] K.-J. Bathe, *Finite element procedures*, Klaus-Jurgen Bathe, Watertown, MA, 2006.

[2] D. Boffi, *Finite element approximation of eigenvalue problems*, Acta Numer. **19** (2010) 1–120.

[3] S.C. Brenner, L.R. Scott, *The mathematical theory of finite element methods*, Springer, New York, 3rd ed., 2008.

[4] M. Bužančić, K. Cherednichenko, I. Velčić, J. Žubrinić, *Spectral and evolution analysis of composite elastic plates with high contrast*, J. Elasticity **152** (2022) 79–177.

[5] E. Carrera, *Historical review of zig-zag theories for multilayered plates and shells*, Appl. Mech. Rev. **56** (2003) 287–308.

[6] P.G. Ciarlet, *Mathematical elasticity, volume I: three-dimensional elasticity*, North-Holland, Amsterdam, 1988.

[7] G.R. Cowper, *Gaussian quadrature formulas for triangles*, Internat. J. Numer. Methods Engrg. **7** (1973) 405–408.

[8] M. Dorduncu, A. Kutlu, E. Madenci, *Triangular C0 continuous finite elements based on refined zigzag theory 2,2 for free and forced vibration analyses of laminated plates*, Compos. Struct. **281** (2022) 115058.

[9] X. Fang, Q. He, H. Ma, C. Zhu, *Multi-field coupling and free vibration of a sandwiched functionally-graded piezoelectric semiconductor plate*, Appl. Math. Mech. (English Ed.) **44** (2023) 1351–1366.

[10] T. Furtmüller, C. Adam, *A higher-order plate theory for the analysis of vibrations of thick orthotropic laminates*, Acta Mech. **233** (2022) 3941–3956.

[11] R. Gulia, A. Garg, V. Sahu, L. Li, *Free vibration and buckling analysis of functionally graded hybrid reinforced laminated composite plates under thermal conditions*, J. Compos. Sci. **9** (2025) 94.

[12] A. Hadrich, S. Zghal, S. Koubaa, Z. Bouaziz, *Free vibration of functionally graded porous perforated solid structures with complex shaped holes*, Internat. J. Solids Structures **319** (2025) 113449.

[13] T.Y. Hou, X.-H. Wu, *A multiscale finite element method for elliptic problems in composite materials and porous media*, J. Comput. Phys. **134** (1997) 169–189.

[14] T.J.R. Hughes, *The finite element method: linear static and dynamic finite element analysis*, Prentice-Hall, Englewood Cliffs, NJ, 1987.

[15] G. Jin, G. Chen, Z. Zhao, Z. Zhao, L. Liu, J. Qian, *Preparation of a superior damping coating and study on vibration damping properties*, SN Appl. Sci. **5** (2023) 220.

[16] P.K. Karsh, A. Alok, J.K. Prusty, V. Dave, M.K. Padhiyar, R.R. Kumar, *Monte Carlo-based stochastic free vibration analysis of bi-directional functionally graded plates*, J. Mech. Sci. Technol. **40** (2026) 5717–5727.

[17] G. Kerschen, J.-C. Golinval, A.F. Vakakis, L.A. Bergman, *The method of proper orthogonal decomposition for dynamical characterization and order reduction of mechanical systems: an overview*, Nonlinear Dynam. **41** (2005) 147–169.

[18] S. Kwak, K. Kim, J. Kim, Y. Kim, Y. Kim, K. Pang, *A meshfree approach for free vibration analysis of laminated sectorial and rectangular plates with varying fiber angle*, Thin-Walled Struct. **174** (2022) 109070.

[19] M.G. Larson, F. Bengzon, *The finite element method: theory, implementation, and applications*, volume 10 of *Texts in Computational Science and Engineering*, Springer, Berlin, Heidelberg, 2013.

[20] R.B. Lehoucq, D.C. Sorensen, C. Yang, *ARPACK users' guide: solution of large-scale eigenvalue problems with implicitly restarted Arnoldi methods*, SIAM, Philadelphia, 1998.

[21] M. Li, C. Guedes Soares, Z. Liu, P. Zhang, *Free and forced vibration analysis of carbon/glass hybrid composite laminated plates under arbitrary boundary conditions*, Appl. Compos. Mater. **31** (2024) 1687–1710.

[22] D. Liu, Z. Tang, Y. Bao, H. Li, *Machine-learning-based methods for output-only structural modal identification*, Struct. Control Health Monit. **28** (2021) e2843.

[23] N. Magouh, L. Azrar, K. Alnefaie, *Semi-analytical solutions of static and dynamic degenerate, nondegenerate and functionally graded electro-elastic multilayered plates*, Appl. Math. Model. **114** (2023) 722–744.

[24] H. Mohammadi, *Isogeometric free vibration analysis of trapezoidally corrugated FG-GRC laminated panels using higher-order shear deformation theory*, Structures **48** (2023) 642–656.

[25] V. Mugnaini, L. Zanotti Fragonara, M. Civera, *A machine learning approach for automatic operational modal analysis*, Mech. Syst. Signal Process. **170** (2022) 108813.

[26] E.C. Onyibo, A. Gazioglu, M. Abulibdeh, O.M. Osman, T.B. Huwail, M. Alkhatib, A. Aburemeis, S. Razavi, S. Sahmani, B. Safaei, *Optimization analysis of stiffness and natural frequency of unidirectional and randomly oriented short fiber-reinforced composite materials*, Acta Mech. **236** (2025) 1935–1953.

[27] A. Pagani, R. Azzara, E. Carrera, *Geometrically nonlinear analysis and vibration of in-plane-loaded variable angle tow composite plates and shells*, Acta Mech. **234** (2023) 85–108.

[28] L. Pan, Y. Zhao, T. Xing, Y. Yuan, *Free vibration of FML beam considering temperature-dependent property and interface slip*, Buildings **15** (2025) 3575.

[29] S.S. Rao, *Vibration of continuous systems*, John Wiley & Sons, Hoboken, NJ, 2007.

[30] J.N. Reddy, *Mechanics of laminated composite plates and shells: theory and analysis*, CRC Press, Boca Raton, 2nd ed., 2004.

[31] R. Selvaraj, K. Gupta, S.K. Singh, A. Patel, M. Ramamoorthy, *Free vibration characteristics of multi-core sandwich composite beams: experimental and numerical investigation*, Polym. Polym. Compos. **29** (2021) S1414–S1423.

[32] G.W. Stewart, *A Krylov–Schur algorithm for large eigenproblems*, SIAM J. Matrix Anal. Appl. **23** (2002) 601–614.

[33] S.P. Timoshenko, D.H. Young, W. Weaver, *Vibration problems in engineering*, John Wiley & Sons, New York, 4th ed., 1974.

[34] Y. Wang, X. Liu, Z. Li, Z. Feng, C. Pan, J. Zhang, J. Xu, *Nitsche-based isogeometric approach for free vibration analysis of laminated plate with multiple stiffeners and cutouts*, Int. J. Mech. Sci. **244** (2023) 108041.

[35] Q. Zang, J. Liu, W. Ye, F. Yang, G. Lin, *A novel isogeometric scaled boundary finite element method for bending and free vibration analyses of laminated plates with rectilinear and curvilinear fibers constrained or free from elastic foundations*, Eng. Anal. Bound. Elem. **154** (2023) 197–222.

[36] T. Zhao, M.J. Bayat, A. Kalhori, K. Asemi, *Free vibration analysis of functionally graded multi-layer hybrid composite cylindrical shell panel reinforced by GPLs and CNTs surrounded by Winkler elastic foundation*, Eng. Struct. **308** (2024) 117975.

[37] Y. Zhou, Y. Gu, J. Lin, H. Zhao, S. Liu, Z. Xu, H. Yu, X. Fu, *Finite element analysis and experimental study on the cutting mechanism of SiCp/Al composites by ultrasonic vibration-assisted cutting*, Ceram. Int. **48** (2022) 35406–35421.

[38] O.C. Zienkiewicz, R.L. Taylor, *The finite element method for solid and structural mechanics*, Elsevier Butterworth-Heinemann, Oxford, 6th ed., 2005.